InSAR slip rate determination on the Altyn Tagh Fault, northern Tibet, in the presence of topographically correlated atmospheric delays

J. R. Elliott,[1] J. Biggs,[1,2] B. Parsons,[1] and T. J. Wright[3]

[1]   The interseismic strain across the Altyn Tagh Fault at 85°E has been measured using 59 interferograms from 26 ERS-1/2 SAR acquisitions on a single track for the period 1993–2000. Using an atmospheric delay correction that scales linearly with height, we estimate the left-lateral strike-slip motion to be $11 \pm_{1\sigma} 5$ mm/yr, assuming no relative vertical motion and a 15 km fault locking depth. This is in agreement with sparse GPS measurements. The atmospheric delay corrections agree well with coarse contemporaneous modelled weather data, reinforcing the importance of correcting for atmospheric delays in InSAR studies of interseismic strain accumulation, particularly in areas of high topographic relief that strongly correlate with the expected tectonic signal. We also find that, in addition to the tropospheric water vapour 'wet' delay, the hydrostatic 'dry' delay makes a significant contribution to the signal. **Citation:** Elliott, J. R., J. Biggs, B. Parsons, and T. J. Wright (2008), InSAR slip rate determination on the Altyn Tagh Fault, northern Tibet, in the presence of topographically correlated atmospheric delays, *Geophys. Res. Lett.*, *35*, L12309, doi:10.1029/2008GL033659.

1.   Introduction

[2]   The 2000-km-long Altyn Tagh Fault (ATF) of northern Tibet marks a major topographic feature separating the low-lying Tarim Basin from the high Tibetan Plateau (Figure 1). There are two end-member views of how continental deformation in Tibet accommodates the Indian sub-continent collision with Asia: (1) as the relative motion of quasi-rigid crustal blocks, with deformation localised on the major faults bounding the blocks [*Avouac and Tapponnier*, 1993; *Thatcher*, 2007] and (2) as mainly ductile deformation continuously distributed throughout the lower continental lithosphere with the brittle upper crust matching the deformation through failure on the myriad faults that exist within it [*England and Houseman*, 1986; *England and Molnar*, 2005]. Accurate fault slip rate determination is key to discriminating between these models. To date there is no consensus for the ATF. Geodetic estimates cluster around 10 mm/yr [*Wallace et al.*, 2004; *Zhang et al.*, 2007; *Jolivet et al.*, 2008], whereas Quaternary dating methods give ~20 mm/yr [*Mériaux et al.*, 2004, 2005], though an alternative interpretation of some of these observations yields rates closer to those from GPS [*Cowgill*, 2007; *Zhang et al.*, 2007], leaving open the question as to whether the disparity arises from uncertainties in the methods, or that the slip rate varies over time.

[3]   InSAR measurements of interseismic strain accumulation rates of mm/yr require multiple interferograms due to the small signal-to-noise ratio [*Peltzer et al.*, 2001; *Wright et al.*, 2001, 2004; *Fialko*, 2006]. The largest perturbing factor limiting accuracy is atmospheric delay, particularly from tropospheric water vapour [e.g., *Puysségur et al.*, 2007]. This is exacerbated for the ATF due to relief of up to 4 km across it. Crustal deformation signals measured over short time scales are dominated by orbital and atmospheric errors. We find standard stacking techniques do not remove topographically correlated atmospheric delay. However, using an networked-interferogram approach, we demonstrate that these errors can be removed.

2.   Estimating Slip-Rates Using InSAR

[4]   We perform differential interferometry on data for a 100 km section along the ATF at 85°E where the topography suggests the fault is a single strand. There are 26 suitable ERS-1/2 acquisitions for 1993–2000 (see Figure S1 and Table S1).[1] Only SAR image pairs with baselines <150 m are used (to avoid topographic decorrelation); these cover time spans up to 5.5 yrs. ERS-2 acquisitions after late 2000 were not used because of satellite gyroscope malfunction. The interferograms were processed using the JPL/Caltech ROI_PAC software [*Rosen et al.*, 2004] and Delft precise orbits, multi-looked to 8 looks (160 m spacing), filtered using a power spectrum filter [*Goldstein and Werner*, 1998] and unwrapped using the branch cut method. Some interferograms required manual unwrapping across the fault due to the loss of coherence. To remove any phase ambiguity, we checked that interferograms sum to zero in a closed loop.

2.1.   Long Period Interferogram Stacking

[5]   An established approach for improving the signal-to-noise ratio of interseismic signals is to stack together many long-interval, short-baseline interferograms in an attempt to reduce uncorrelated noise [*Wright et al.*, 2001, 2004; *Fialko*, 2006]. Utilising the six longest-period independent interferograms with a cumulative time span of 22 yrs, we calculate a line-of-sight deformation rate (Figure S2). We assume pure strike-slip motion for this section of the fault with no vertical component of motion,

---

[1]COMET, Department of Earth Sciences, University of Oxford, Oxford, UK.
[2]Now at RSMAS, University of Miami, Florida, USA.
[3]COMET, School of Earth and Environmental Sciences, University of Leeds, Leeds, UK.
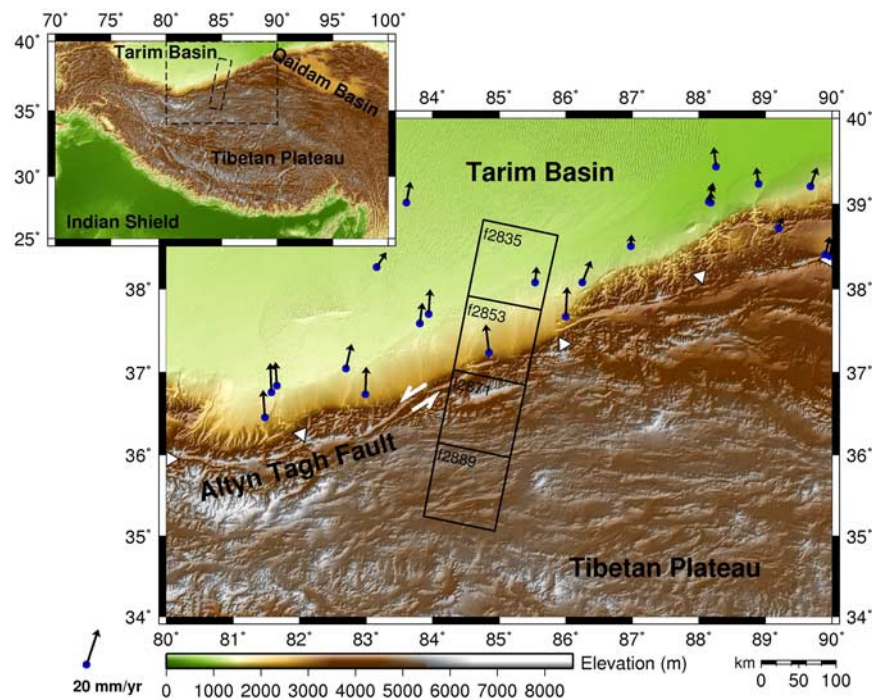
Figure 1. Elevation map of northern Tibet with Tibetan Plateau inset. The left-lateral strike-slip ATF, delineated by white triangles, clearly bounds the low lying 1 km elevation Tarim Basin from the 5 km high plateau. Black boxes mark the 100 km wide SAR coverage for the ERS descending satellite track 391. GPS vectors compiled from [*Shen et al.*, 2001; *Wang et al.*, 2001; *Wallace et al.*, 2004; *Zhang et al.*, 2004], relative to a fixed Eurasia. Note lack of GPS data south of the fault in this western region, an area ~1000 km by 400 km.

supported by a lack of evidence for thrusting comparable to that further east (Figure 1). If incorrect, any uplift on the southern side of the fault would be interpreted as left-lateral slip. Hence our estimate would be higher than the true rate. This rate is calculated using a simple model of the fault as a screw dislocation in an elastic half space locked to 15 km depth [*Savage and Burford*, 1973], and no corrections are made for orbital or atmospheric errors. We find a yearly phase change across the fault consistent with 44 mm/yr of horizontal, left-lateral strike slip motion (Figure S2). This estimate is large, even compared to the highest Quaternary slip rate estimates [*Mériaux et al.*, 2004] and we suspect this is caused by unmodelled atmospheric delay. Individual interferograms show a strong correlation with topography (Figure S3) and modelled weather data from the European Centre for Medium Range Weather Forecasting (ECMWF) show strong seasonal variations in topographically-correlated water vapour.

2.2. Network Orbital Correction

[6] This method follows the small baseline approach [*Berardino et al.*, 2002] and employs a network approach to remove orbital errors [*Biggs et al.*, 2007]. The latter uses information in all 59 interferograms, allowing orbital errors to be estimated at each epoch rather than for each interferogram, but requires interferograms be downsampled to 4 km pixels to limit the computational cost. The inversion is underdetermined so we use SVD to give the minimum norm solution, but biases may remain in the orbital parameters. The orbital correction comprises a 2-D linear ramp estimated only from data more than 50 km south of the fault. Here relief is small and at high altitude so water

vapour variations are small, as are deformation gradients at this distance from the fault. Data from the most southerly SAR frame (2889) are used if available (50% of interferograms). Data north of the fault is not used as there is little coherence away from the fault in the Tarim Basin.

[7] Using the 25 most coherent corrected interferograms connecting the 26 epochs, we invert for the rate of displacement on a pixel-by-pixel basis, using only pixels coherent in all interferograms. The inversion is weighted by a variance-covariance matrix that accounts for the common epochs in the set of interferograms and is scaled by the median variance calculated from all interferograms.

[8] Using the rate map obtained in this way (Figure S4), we solve for the slip rate on a vertical fault locked to 15 km in addition to a final orbital adjustment. This inversion is weighted by a variance-covariance matrix which takes into account the spatial correlation between pixels in the rate-map, assuming an exponentially-decaying form for the covariance, with a length scale of 12.3 km (calculated from the median auto-covariance functions for all interferograms). This yields a rate of 35 mm/yr with a formal error of 3 mm/yr, still higher than Quaternary slip rate estimates.

2.3. Network Atmospheric Correction

[9] To remove topographically correlated atmospheric path delays we apply a further network correction to the flattened interferograms, assuming the path delays vary linearly with height as a first-order approximation [e.g., *Wicks et al.*, 2002; *Cavalié et al.*, 2007]. MEdium Resolution Imaging Spectrometer (MERIS) water vapour data for this track on selected dates between 2002–07 indicate exponential decay relationships with height, but with linear fits
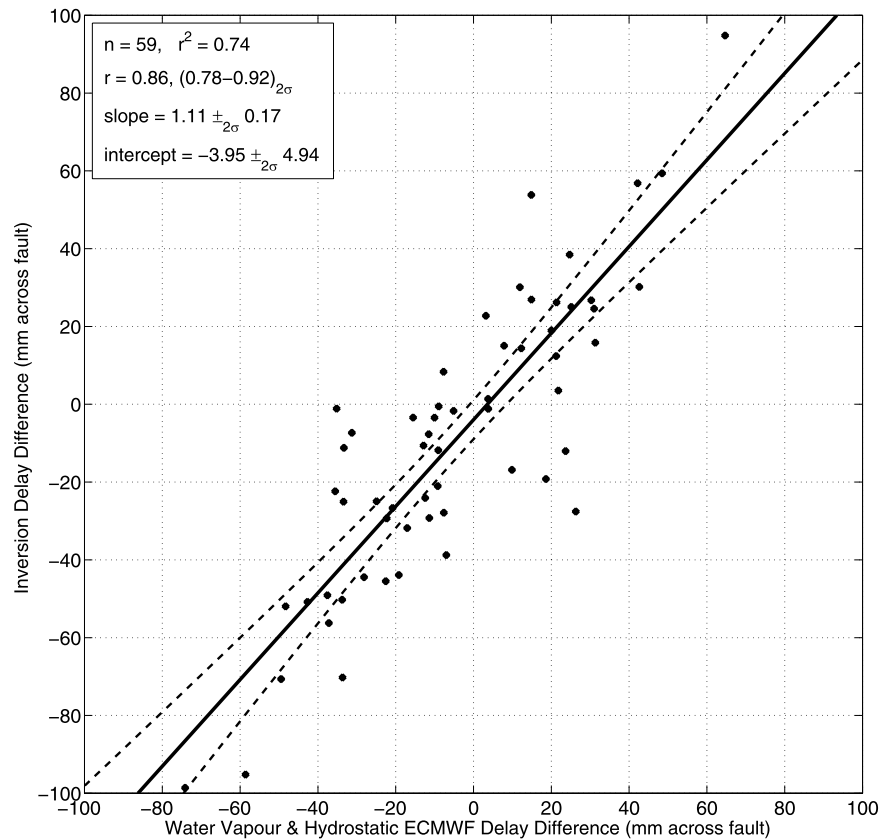
Figure 2. Correlation between the atmospheric path delay solved for in the network inversion and the total path delay difference calculated from the ECMWF modelled water vapour and pressure data. The linear regression line is marked in solid with the dashed lines indicating the 2σ range. A strong positive correlation is found with a slope of 1 within 2σ error.

giving a reasonable approximation. Figure S5 shows the interferogram profiles before and after the corrections are made. The estimated path delays were compared with ECMWF data for the region available at $1°$ resolution every six hours. Using the total column water vapour from this data set, a line-of-sight phase delay can be estimated [*Bevis et al.*, 1992]. When the relative path delay across the fault from the network atmospheric correction is compared to that estimated from the modelled water vapour delay, a strong correlation ($r = 0.65$) is observed (Figure S6). However, a much stronger correlation ($r = 0.86$) is found if the hydrostatic delay [*Davis et al.*, 1985], proportional to changes in air pressure between acquisitions, is also included (Figure 2). This much improved correlation suggests the hydrostatic delay can make a significant contribution to the total tropospheric path delay and should be accounted for along with the water vapour delay [*Puysségur et al.*, 2007].

### 2.4. Formation of Ratemap and Final Inversion for Slip Rate

[10] A line-of-sight rate map is calculated from the interferograms corrected for both orbital errors and total tropospheric path delays in the same manner as described in sections 2.2 and 2.3. A final inversion to solve for a slip rate, in addition to a planar orbital and linear atmospheric correction for any residual errors, yields 10.6 mm/yr with a formal one-sigma error of 3.4 mm/yr. Figure 3a shows the line-of-sight rate map with the final orbital and atmospheric

corrections removed. Rates predicted by the fault model for the best-fitting slip rate, and the difference between the observed and predicted rate maps, are shown in Figures 3b and 3c, respectively. To test the robustness of the inversion method, Monte Carlo analysis was performed on synthetic data sets with characteristic orbital and atmospheric errors added. This analysis shows the method is insensitive to seasonal biases from water vapour, but yields a more realistic estimate of error, giving a slip rate of $11 \pm_{1\sigma} 5$ mm/yr.

3. Discussion

[11] The inversion for slip is performed assuming a 15 km locking depth. However, there is a trade-off between the locking depth and calculated slip rate (Figure S7). The rms misfit for the range of solutions obtained by varying the input locking depth shows a broad minimum in the locked depth range of $10-20$ km. Locking depths >20 km are not consistent with slip distributions from co-seismic studies for recent large Tibetan earthquakes [e.g., *Lasserre et al.*, 2005]. Further east along the ATF at $94°$E, [*Jolivet et al.*, 2008] obtain a lower locking depth of $7-9$ km and a similar slip rate of $8-10$ mm/yr. However, due to the paucity of data near the fault, and therefore a poorly constrained locking depth in this study, we cannot conclude that this value is significantly different.

[12] An asymmetry is noted in the rate map (Figure 3) with an offset in the maximum deformation gradient
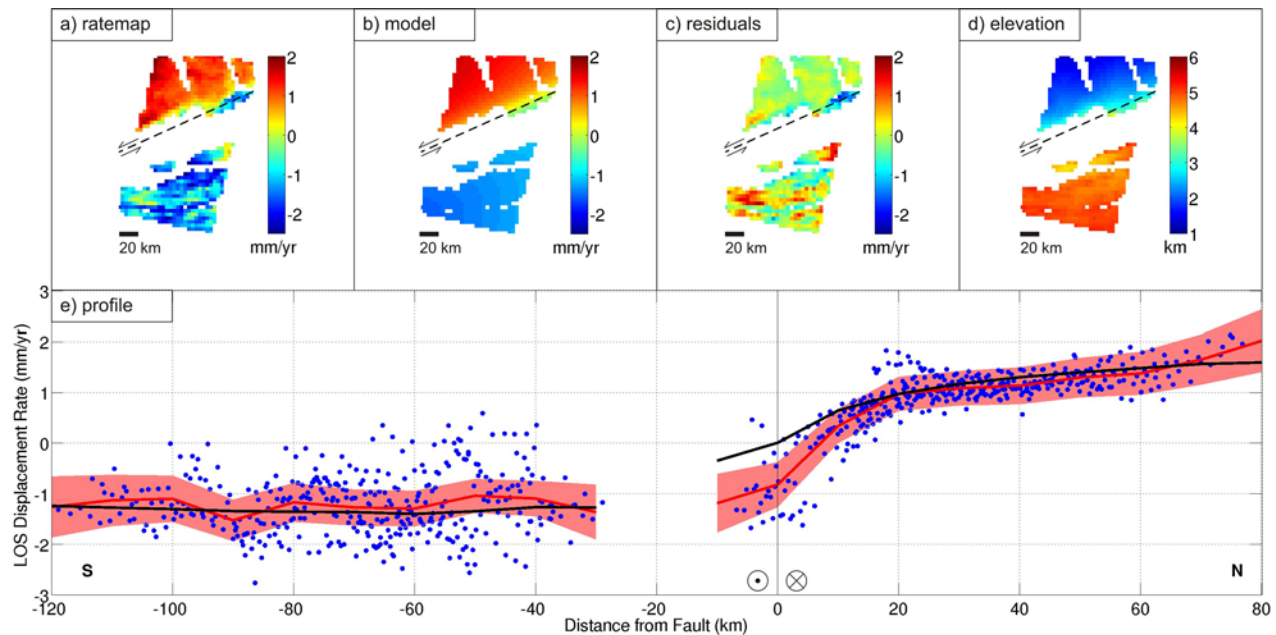
Figure 3. (a) Line-of-sight ratemap from the inversion of 25 interferograms connecting all epochs, with the final orbital and atmospheric corrections made. Positive values indicate motion away from the satellite and the arbitrary null LOS displacement point is taken at the fault. (b) Modelled ratemap for a slip rate of 10.6 mm/yr solved for in the final inversion. The final orbital and atmospheric corrections have been made. (c) Residuals between data and model, (d) elevation, and (e) profile perpendicular to fault with data from the ratemap marked as blue dots, a 10 km moving average line of the data (red) and model (black). The red band indicates the 1-sigma error range for the mean profile, calculated using the ratemap error and spatial correlation between pixels.

~10 km northwards of the fault. Similar asymmetries are noted elsewhere on the ATF [*Jolivet et al.*, 2008] and on the San Andreas Fault [*Fialko*, 2006]. However, the sense of asymmetry here is in the opposite direction to that expected for a more rigid Tarim Basin. A dip in the fault to the south away from the assumed vertical would also give the opposite sense of asymmetry, so this observation remains unexplained.

[13] Our result is in good agreement with GPS measurements of 10 mm/yr [*Wallace et al.*, 2004; *Zhang et al.*, 2007] for the central ATF, but differs significantly from rates determined by Quaternary dating methods [*Mériaux et al.*, 2004] at the same longitude of 27 ± 7 mm/yr. However, an alternative interpretation of the model used to calculate the Quaternary slip rate, given by *Mériaux et al.* [2004] themselves, yields an estimate of 18.4 ± 3.3 mm/yr, in addition to the reinterpretations given by *Zhang et al.* [2007] of 8–12 mm/yr. Fault slip rates have been shown to vary with time in Southern California [*Dolan et al.*, 2007], but current uncertainties in the two methods used to estimate slip rates, do not allow us to conclude that motion varies over time for the ATF.

[14] The present-day slip rates measured by InSAR along the ATF from the west [*Wright et al.*, 2004] (0–10 mm/yr), through the centre [this study] (6–16 mm/yr), to the east [*Jolivet et al.*, 2008] (8–10 mm/yr) do not show any systematic variations along strike, with estimates clustering around 10 mm/yr, before decreasing east of 96°E [*Zhang et al.*, 2007]. These results are consistent with the ATF playing only a limited role in the north-eastward extrusion of material in the Tibetan Plateau [*Zhang et al.*, 2007], with

most of the extrusion occurring in the interior of the plateau, and they support recent dynamical models of Asian deformation requiring low fault slip rates [e.g., *England and Molnar*, 2005; *Vergnolle et al.*, 2007].

References

Avouac, J.-P., and P. Tapponnier (1993), Kinematic model of active deformation in central Asia, *Geophys. Res. Lett.*, *20*, 895–898.

Berardino, P., G. Fornaro, R. Lanari, and E. Sansosti (2002), A new algorithm for surface deformation monitoring based on small baseline differential SAR interferograms, *IEEE Trans. Geosci. Remote Sens.*, *40*, 2375–2383, doi:10.1109/TGRS.2002.803792.

Bevis, M., S. Businger, T. A. Herring, C. Rocken, R. A. Anthes, and R. H. Ware (1992), GPS meteorology: Remote sensing of atmospheric water vapor using the Global Positioning System, *J. Geophys. Res.*, *97*, 15,787–15,801.

Biggs, J., T. Wright, Z. Lu, and B. Parsons (2007), Multi-interferogram method for measuring interseismic deformation: Denali fault, Alaska, *Geophys. J. Int.*, *170*, 1165–1179, doi:10.1111/j.1365-246X.2007.03415.x.

Cavalié, O., M.-P. Doin, C. Lasserre, and P. Briole (2007), Ground motion measurement in the Lake Mead area, Nevada, by differential synthetic aperture radar interferometry time series analysis: Probing the lithosphere rheological structure, *J. Geophys. Res.*, *112*, B03403, doi:10.1029/2006JB004344.

Cowgill, E. (2007), Impact of riser reconstructions on estimation of secular variation in rates of strike slip faulting: Revisiting the Cherchen River site along the Altyn Tagh Fault, NW China, *Earth Planet. Sci. Lett.*, *254*, 239–255, doi:10.1016/j.epsl.2006.09.015.

Davis, J. L., T. A. Herring, I. I. Shapiro, A. E. E. Rogers, and G. Elgered (1985), Geodesy by radio interferometry: Effects of atmospheric modeling errors on estimates of baseline length, *Radio Sci.*, *20*, 1593–1607.

Dolan, J. F., D. D. Bowman, and C. G. Briole (2007), Long-range and long-term fault interactions in southern California, *Geology*, *35*, 855–858, doi:10.1130/G23789A.

England, P., and G. Houseman (1986), Finite strain calculations of continental deformation: 2. Comparison with the India-Asia collision zone, *J. Geophys. Res.*, *91*, 3664–3676.

England, P., and P. Molnar (2005), Late Quaternary to decadal velocity fields in Asia, *J. Geophys. Res.*, *110*, B12401, doi:10.1029/2004JB003541.

Fialko, Y. (2006), Interseismic strain accumulation and the earthquake potential on the southern San Andreas fault system, *Nature*, *441*, 968–971, doi:10.1038/nature04797.

Goldstein, R. M., and C. L. Werner (1998), Radar interferogram filtering for geophysical applications, *Geophys. Res. Lett.*, *25*, 4035–4038, doi:10.1029/1998GL900033.

Jolivet, R., R. Cattin, N. Chamot-Rooke, C. Lasserre, and G. Peltzer (2008), Thin-plate modeling of interseismic deformation and asymmetry across the Altyn Tagh fault zone, *Geophys. Res. Lett.*, *35*, L02309, doi:10.1029/2007GL031511.

Lasserre, C., G. Peltzer, F. Crampé, Y. Klinger, J. Van der Woerd, and P. Tapponnier (2005), Coseismic deformation of the 2001 M_w = 7.8 Kokoxili earthquake in Tibet, measured by synthetic aperture radar interferometry, *J. Geophys. Res.*, *110*, B12408, doi:10.1029/2004JB003500.

Mériaux, A.-S., F. J. Ryerson, P. Tapponnier, J. Van der Woerd, R. C. Finkel, X. Xu, Z. Xu, and M. W. Caffee (2004), Rapid slip along the central Altyn Tagh Fault: Morphochronologic evidence from Cherchen He and Sulamu Tagh, *J. Geophys. Res.*, *109*, B06401, doi:10.1029/2003JB002558.

Mériaux, A.-S., et al. (2005), The Aksay segment of the northern Altyn Tagh Fault: Tectonic geomorphology, landscape evolution, and Holocene slip rate, *J. Geophys. Res.*, *110*, B04404, doi:10.1029/2004JB003210.

Peltzer, G., F. Crampé, S. Hensley, and P. Rosen (2001), Transient strain accumulation and fault interaction in the eastern California shear zone, *Geology*, *29*, 975–978, doi:10.1130/0091-7613(2001)029<0975:TSAAFI>2.0. CO;2.

Puysségur, B., R. Michel, and J.-P. Avouac (2007), Tropospheric phase delay in interferometric synthetic aperture radar estimated from meteorological model and multispectral imagery, *J. Geophys. Res.*, *112*, B05419, doi:10.1029/2006JB004352.

Rosen, P. A., S. Henley, G. Peltzer, and M. Simons (2004), Update repeat orbit interferometry package released, *Eos Trans. AGU*, *85*, 47, doi:10.1029/2004EO050004.

Savage, G. D., and R. O. Burford (1973), Geodetic determination of relative plate motion in central California, *J. Geophys. Res.*, *5*, 832–845.

Shen, Z.-K., M. Wang, Y. Li, D. D. Jackson, A. Yin, D. Dong, and P. Fang (2001), Crustal deformation along the Altyn Tagh fault system, western China, from GPS, *J. Geophys. Res.*, *106*, 30,607–30,622, doi:10.1029/2001JB000349.

Thatcher, W. (2007), Microplate model for the present-day deformation of Tibet, *J. Geophys. Res.*, *112*, B01401, doi:10.1029/2005JB004244.

Vergnolle, M., E. Calais, and L. Dong (2007), Dynamics of continental deformation in Asia, *J. Geophys. Res.*, *112*, B11403, doi:10.1029/2006JB004807.

Wallace, K., G. Yin, and R. Bilham (2004), Inescapable slow slip on the Altyn Tagh Fault, *Geophys. Res. Lett.*, *31*, L09613, doi:10.1029/2004GL019724.

Wang, Q., et al. (2001), Present-day crustal deformation in China constrained by Global Positioning System measurements, *Science*, *294*, 574–578, doi:10.1126/science.1063647.

Wicks, C. W., D. Dzurisin, S. Ingebritsen, W. Thatcher, Z. Lu, and J. Iverson (2002), Magmatic activity beneath the quiescent Three Sisters volcanic center, central Oregon Cascade Range, USA, *Geophys. Res. Lett.*, *29*(7), 1122, doi:10.1029/2001GL014205.

Wright, T., B. Parsons, and E. Fielding (2001), Measurement of interseismic strain accumulation across the North Anatolian Fault by satellite radar interferometry, *Geophys. Res. Lett.*, *28*, 2117–2120, doi:10.1029/2000GL012850.

Wright, T. J., B. Parsons, P. C. England, and E. J. Fielding (2004), InSAR observations of low slip rates on the major faults of western Tibet, *Science*, *305*, 236–239, doi:10.1126/science.1096388.

Zhang, P.-Z., et al. (2004), Continuous deformation of the Tibetan Plateau from Global Positioning System data, *Geology*, *32*, 809–812, doi:10.1130/G20554.1.

Zhang, P. Z., P. Molnar, and X. Xu (2007), Late Quaternary and present-day rates of slip along the Altyn Tagh Fault, northern margin of the Tibetan Plateau, *Tectonics*, *26*, TC5010, doi:10.1029/2006TC002014.

_____

J. Biggs, RSMAS, Rickenbacker Causeway, University of Miami, FL 33149, USA.

J. R. Elliott and B. Parsons, Department of Earth Sciences, University of Oxford, Parks Road, Oxford OX1 3PR, UK. (john.elliott@earth.ox.ac.uk)

T. J. Wright, School of Earth and Environmental Sciences, University of Leeds, Leeds LS2 9JT, UK.